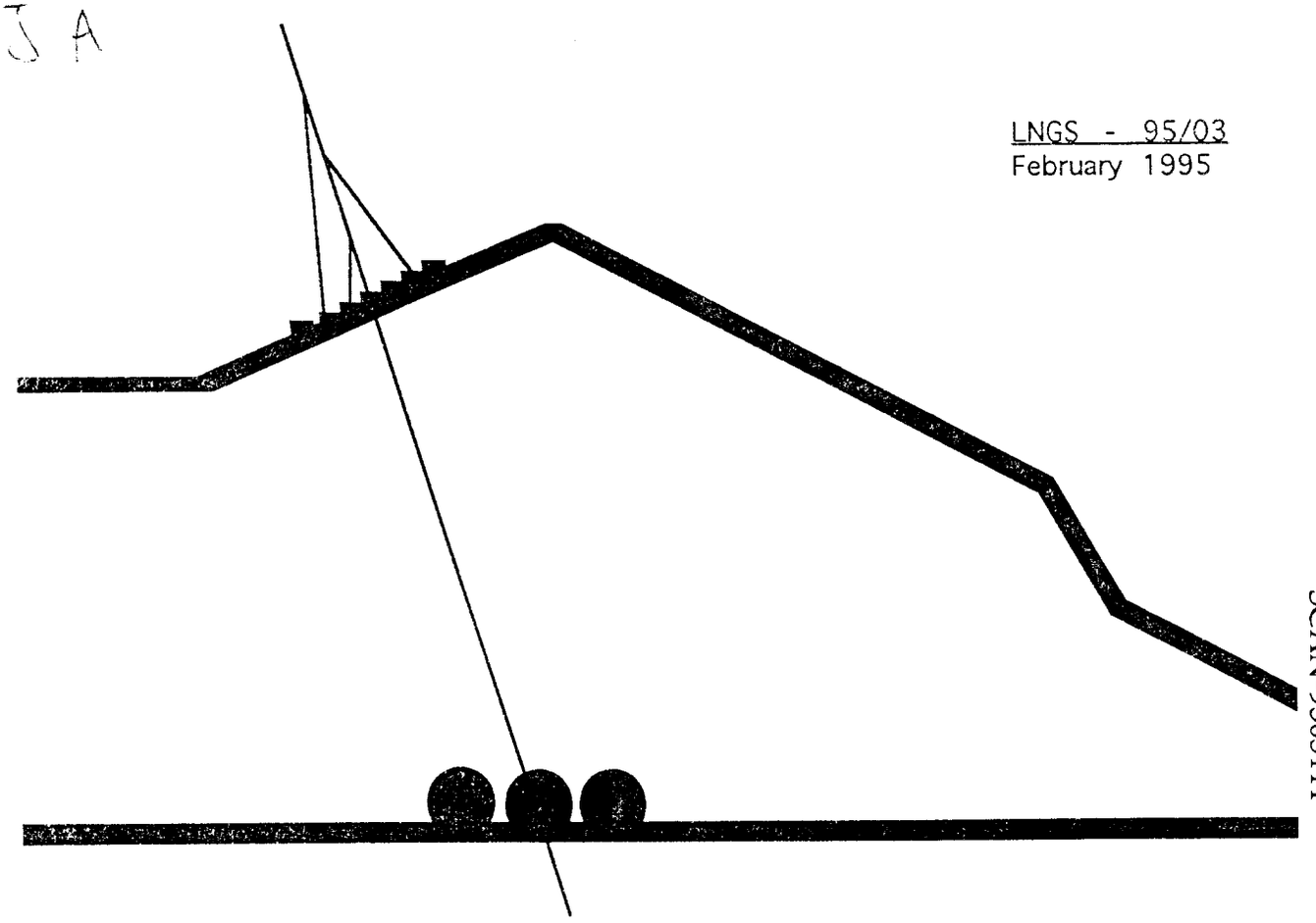

LNGS - 95/03
February 1995

Vertical Muon Intensity Measured with MACRO at Gran Sasso Laboratory

The MACRO Collaboration

INFN - Laboratori Nazionali del Gran Sasso

LNGS - 95/03
February 1995

Vertical Muon Intensity Measured with MACRO at the Gran Sasso Laboratory

The MACRO Collaboration

M. Ambrosio[12], R. Antolini[7], G. Auriemma[14,a], R. Baker[11], A. Baldini[13], G. C. Barbarino[12], B. C. Barish[4], G. Battistoni[6,b], R. Bellotti[1], C. Bemporad[13], P. Bernardini[10], H. Bilokon[6], V. Bisi[16], C. Bloise[6], C. Bower[8], S. Bussino[14], F. Cafagna[1], M. Calicchio[1], D. Campana[12], M. Carboni[6]. M. Castellano[1], S. Cecchini[2,c], F. Cei[13,d], P. Celio[14], V. Chiarella[6], A. Corona[14], S. Coutu[11], G. De Cataldo[1], H. Dekhissi[2,e], C. De Marzo[1], I. De Mitri[9], M. De Vincenzi[14,f], A. Di Credico[7,14], O. Erriquez[1], C. Favuzzi[1], C. Forti[6], P. Fusco[1], G. Giacomelli[2], G. Giannini[13,g], N. Giglietto[1], M. Grassi[13], A. Grillo[7], F. Guarino[12], P. Guarnaccia[1], C. Gustavino[7], A. Habig[8], K. Hanson[11], A. Hawthorne[8], R. Heinz[8], J. T. Hong[3], E. Iarocci[6,h], E. Katsavounidis[4], E. Kearns[3], S. Kyriazopoulou[4], E. Lamanna[14], C. Lane[5], D. S. Levin[11], P. Lipari[14], R. Liu[4], N. Longley[4], M. J. Longo[11], Y. Lu[15], G. Ludlam[3], G. Mancarella[10], G. Mandrioli[2], A. Margiotta-Neri[2], A. Marini[6], D. Martello[10], A. Marzari-Chiesa[16], M. N. Mazziotta[1], D. G. Michael[4], S. Mikheyev[7,i], L. Miller[8], M. Mittelbrunn[5], P. Monacelli[9], T. Montaruli[1], M. Monteno[16], S. Mufson[8], J. Musser[8], D. Nicoló[13,d], R. Nolty[4], C. Okada[3], C. Orth[3], G. Osteria[12]. O. Palamara[10], S. Parlati[7], V. Patera[6,h], L. Patrizii[2], R. Pazzi[13], C. W. Peck[4], S. Petrera[10], N. D. Pignatano[4], P. Pistilli[10], V. Popa[2,l], A. Rainó[1], J. Reynoldson[7], F. Ronga[6], A. Sanzgiri[15], F. Sartogo[14], C. Satriano[14,a], L. Satta[6,h], E. Scapparone[2], K. Scholberg[4], A. Sciubba[6,h], P. Serra-Lugaresi[2], M. Severi[14], M. Sitta[16]. P. Spinelli[1], M. Spinetti[6], M. Spurio[2], R. Steinberg[5], J. L. Stone[3], L.R. Sulak[3], A. Surdo[10], G. Tarlé[11], F. Tassoni[14], V. Togo[2], V. Valente[6], C. W. Walter[4] and R. Webb[15]

1. Dipartimento di Fisica dell'Università di Bari and INFN, 70126 Bari, Italy
2. Dipartimento di Fisica dell'Università di Bologna and INFN, 40126 Bologna, Italy
3. Physics Department, Boston University, Boston, MA 02215, USA
4. California Institute of Technology, Pasadena, CA 91125, USA
5. Department of Physics, Drexel University, Philadelphia, PA 19104, USA
6. Laboratori Nazionali di Frascati dell'INFN, 00044 Frascati (Roma), Italy
7. Laboratori Nazionali del Gran Sasso dell'INFN, 67010 Assergi (L'Aquila), Italy
8. Depts. of Physics and of Astronomy, Indiana University, Bloomington, IN 47405, USA
9. Dipartimento di Fisica dell'Università dell'Aquila and INFN, 67100 L'Aquila, Italy
10. Dipartimento di Fisica dell'Università di Lecce and INFN, 73100 Lecce, Italy
11. Department of Physics, University of Michigan, Ann Arbor, MI 48109, USA
12. Dipartimento di Fisica dell'Università di Napoli and INFN, 80125 Napoli, Italy
13. Dipartimento di Fisica dell'Università di Pisa and INFN, 56010 Pisa, Italy
14. Dipartimento di Fisica dell'Università di Roma "La Sapienza" and INFN, 00185 Roma, Italy
15. Physics Department, Texas A&M University, College Station, TX 77843, USA
16. Dipartimento di Fisica Sperimentale dell'Università di Torino and INFN, 10125 Torino, Italy

a Also Università della Basilicata, 85100 Potenza, Italy
b Also INFN Milano, 20133 Milano, Italy
c Also Istituto TESRE/CNR, 40129 Bologna, Italy
d Also Scuola Normale Superiore di Pisa, 56010 Pisa, Italy
e Also Faculty of Sciences, University Mohamed I, B.P. 424 Oujda, Morocco
f Also Dipartimento di Fisica, Università di Roma III, Roma, Italy
g Also Università di Trieste and INFN, 34100 Trieste, Italy

h Also Dipartimento di Energetica, Università di Roma, 00185 Roma, Italy
i Also Institute for Nuclear Research, Russian Academy of Science, 117312 Moscow, Russia
l Also Institute for Atomic Physics, 76900 Bucharest, Romania

Abstract

We report new results on the vertical muon intensity, on the primary "all-nucleon" spectrum and on the surface muon flux. The data were obtained in $\sim$ 500 days of data taking with the lower MACRO detector at the Gran Sasso Laboratory. A comparison with the world data is also presented.

(Submitted to Phys. Rev. D)
PACS numbers: 13.85.T, 96.40.T

1. Introduction

Measurements of the underground muon intensity still provide the main information on the energy spectrum of atmospheric muons above 1 TeV and yield information on the "all-nucleon" spectrum of the primary cosmic radiation. They also constrain models of atmospheric showers, through both the muon vertical intensity slope and the absolute normalization. Further information on atmospheric processes may be obtained from the measurement of the underground muon intensity versus the zenith angle θ. As suggested by several authors, the production of prompt muons in atmospheric showers should modify the $\sec(\theta)$ angular distribution characteristic of pion and kaon decays and interactions [1, 2, 3].

In this paper we present new measurements of the underground muon intensity in the energy range 1 – 20 TeV, corresponding to a primary energy 10 – 200 TeV/nucleon, performed with the MACRO detector running at the Gran Sasso National Laboratory in central Italy. We use this measurement to extract the primary all nucleon spectrum. The analysis of prompt muon production will be the focus of a further paper.

The rock overburden has a minimum depth of 3150 hg cm^{-2}; its composition and topography are discussed in detail in the Appendix. The detector has been described in detail elsewhere [4], and when completed will have an acceptance of $\sim$ 10000 m^2 sr for isotropic fluxes. A first measurement of single muon data was performed earlier with a limited portion of the detector [5] and a reduced statistics data sample which allowed the measurement of the vertical intensity up to 5200 hg cm^{-2}.

2. Vertical muon intensity

The present analysis refers to data collected with the lower part of MACRO with an acceptance of $S\Omega \simeq 3100$ m^2 sr for atmospheric muons. The lower structure consists of six nearly identical units, called supermodules, of 12m $\times$ 12m $\times$ 4.8m. Each supermodule consists of ten horizontal planes of streamer tubes, 12m $\times$ 12m. The eight innermost planes are separated by seven layers of $\simeq$ 60 g cm^{-2} absorbers of low activity Gran Sasso rock. The two outermost planes are separated by two 19 cm layers

of liquid scintillator. The lateral walls consist of stacked tanks of liquid scintillator, 25 cm thick, sandwiched between six vertical streamer tubes planes.

All streamer tube wires are read out, providing the X coordinate on the horizontal planes and the Z coordinate on the vertical planes. On the horizontal planes the second coordinate, D, is obtained by reading the pulses induced on horizontal aluminum strips oriented at 26.5° with respect to the streamer tubes axis, to allow stereoscopic reconstruction. Muon tracks are thus reconstructed with an angular resolution of 0.2°. This resolution is negligible when compared to the average multiple scattering angle of 0.8° for muons crossing the overburden rock. This value is consistent with the angular differences measured between parallel muons belonging to the same event detected in MACRO.

Data were collected in a 500 day period, starting in July 1991, when the apparatus was still under construction, using only the streamer tube system. The hardware trigger was defined by either six streamer tube planes fired anywhere, or five consecutive horizontal planes, excluding the first and the last ones. A muon track is reconstructed if at least four horizontal planes are recorded, both in the wire and strip views. The data runs were then selected as follows: runs were accepted if they had ≥ 4 hr duration; had a dead time of less than 1%; and a counting rate per hour per supermodule inside a range of $\pm 3\sigma$ around the mean value. After these cuts, we have 3.91×10^6 muons surviving over a live time of 4228 hours. These statistics are thus more than one order of magnitude larger than those reported in Reference [5]. The large statistics of this sample allows us to also study the Gran Sasso rock systematics and to reject angular regions where the muon intensities are not compatible with the measured average intensities of the regions with the same nominal rock thickness.

The total data sample (single and multiple muons) is used to determine the bin-by-bin vertical muon intensity $I(h, \theta, \phi)$ as:

$$I(h, \theta, \phi) = \left(\frac{1}{\Delta T}\right) \frac{\Sigma_i N_i m_i}{\Sigma_j \Delta\Omega_j A_j \epsilon_j / \cos\theta_j} \tag{1}$$

where ΔT is the live time; N_i is the number of observed events of muon multiplicity m_i in the bin of slant depth h, taken from the military topographical map of the mountain described in the Appendix; A_j is the geometric detector projected area for that bin; ϵ_j is the combined trigger and reconstruction efficiency and θ_j is the muon zenith angle. The data is binned with $\Delta\theta = 1°$, $\Delta\phi = 2°$.

The projected area $A_j(\theta, \phi)$ and the detector tracking efficiency $\epsilon_j(\theta, \phi)$ were calculated from a detailed Monte Carlo based on GEANT [6] to produce simulated data which were processed through the same offline chain used for real data. For each bin the Gran Sasso rock thickness in meters was converted to standard rock slant depth (hg cm^{-2}) using the Gran Sasso rock parameters listed in Table 4, and a conversion formula described in Reference [7].

The solid angle bins were then divided into 54 bins of equal slant depth h and width Δh = 50 hg cm^{-2} in the range 3200 < h < 4750 hg cm^{-2}, Δh = 100 hg cm^{-2} thereafter until h = 6950 hg cm^{-2}. The measured vertical muon intensity as a function of the slant depth h, for the zenith range 0° - 60°, is reported in Table 1 and is shown in Figure 1. Each point is the mean value of the $I(h, \theta, \phi)$ distribution at fixed slant depth h.

Depth	$I(h) \pm \Delta I(h)$	Depth	$I(h) \pm \Delta I(h)$
3200	$(2.00 \pm 0.01) \times 10^{-8}$	4550	$(3.29 \pm 0.07) \times 10^{-9}$
3250	$(1.85 \pm 0.01) \times 10^{-8}$	4600	$(3.05 \pm 0.07) \times 10^{-9}$
3300	$(1.73 \pm 0.01) \times 10^{-8}$	4650	$(2.92 \pm 0.04) \times 10^{-9}$
3350	$(1.59 \pm 0.01) \times 10^{-8}$	4700	$(2.72 \pm 0.06) \times 10^{-9}$
3400	$(1.48 \pm 0.01) \times 10^{-8}$	4762	$(2.61 \pm 0.04) \times 10^{-9}$
3450	$(1.39 \pm 0.01) \times 10^{-8}$	4850	$(2.32 \pm 0.06) \times 10^{-9}$
3500	$(1.30 \pm 0.01) \times 10^{-8}$	4950	$(2.02 \pm 0.06) \times 10^{-9}$
3550	$(1.215 \pm 0.008) \times 10^{-8}$	5050	$(1.86 \pm 0.03) \times 10^{-9}$
3600	$(1.144 \pm 0.008) \times 10^{-8}$	5150	$(1.60 \pm 0.04) \times 10^{-9}$
3650	$(1.058 \pm 0.007) \times 10^{-8}$	5250	$(1.40 \pm 0.02) \times 10^{-9}$
3700	$(1.000 \pm 0.007) \times 10^{-8}$	5350	$(1.28 \pm 0.04) \times 10^{-9}$
3750	$(9.44 \pm 0.07) \times 10^{-9}$	5450	$(1.05 \pm 0.03) \times 10^{-9}$
3800	$(8.85 \pm 0.06) \times 10^{-9}$	5550	$(9.6 \pm 0.2) \times 10^{-10}$
3850	$(8.23 \pm 0.06) \times 10^{-9}$	5650	$(8.7 \pm 0.2) \times 10^{-10}$
3900	$(7.73 \pm 0.07) \times 10^{-9}$	5750	$(7.5 \pm 0.1) \times 10^{-10}$
3950	$(7.20 \pm 0.07) \times 10^{-9}$	5850	$(6.8 \pm 0.2) \times 10^{-10}$
4000	$(6.75 \pm 0.06) \times 10^{-9}$	5950	$(5.8 \pm 0.5) \times 10^{-10}$
4050	$(6.37 \pm 0.06) \times 10^{-9}$	6050	$(5.2 \pm 0.3) \times 10^{-10}$
4100	$(5.88 \pm 0.06) \times 10^{-9}$	6150	$(4.6 \pm 0.2) \times 10^{-10}$
4150	$(5.49 \pm 0.06) \times 10^{-9}$	6250	$(4.3 \pm 0.1) \times 10^{-10}$
4200	$(5.15 \pm 0.05) \times 10^{-9}$	6350	$(3.6 \pm 0.7) \times 10^{-10}$
4250	$(4.82 \pm 0.06) \times 10^{-9}$	6450	$(3.2 \pm 0.4) \times 10^{-10}$
4300	$(4.51 \pm 0.05) \times 10^{-9}$	6550	$(2.7 \pm 0.3) \times 10^{-10}$
4350	$(4.21 \pm 0.07) \times 10^{-9}$	6650	$(2.7 \pm 0.5) \times 10^{-10}$
4400	$(3.94 \pm 0.07) \times 10^{-9}$	6750	$(2.2 \pm 0.3) \times 10^{-10}$
4450	$(3.69 \pm 0.09) \times 10^{-9}$	6850	$(2.2 \pm 0.3) \times 10^{-10}$
4500	$(3.46 \pm 0.03) \times 10^{-9}$	6950	$(2.0 \pm 0.3) \times 10^{-10}$

Table 1: Measured vertical muon underground intensity in $cm^{-2}\ s^{-1}\ sr^{-1}$. Slant depths are in standard rock (hg cm^{-2}). The quoted errors take into account the statistical uncertainties and the topographical map resolution. The additional estimated systematic scale uncertainty is $\pm 8\%$, see text.

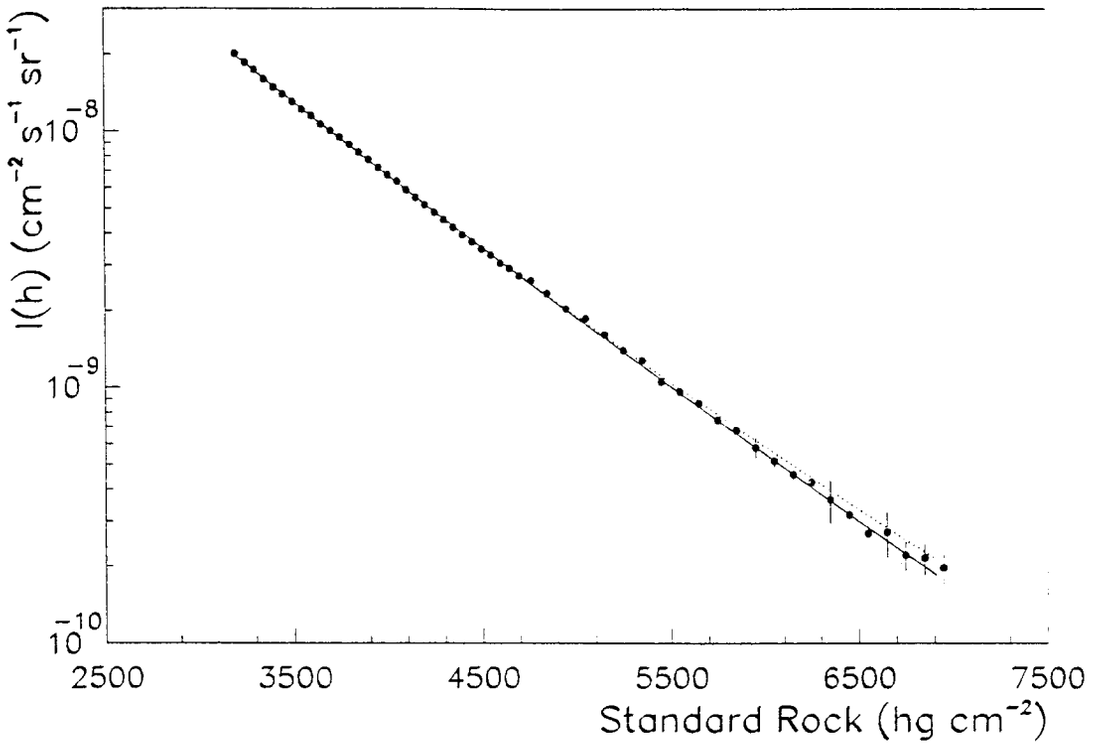

Figure 1: Measured vertical muon intensity versus standard rock (black points). The dotted and solid lines are the two and three parameter fits described in the text.

The study of the point to point uncertainties, due to the knowledge of the topographical map, produced the cut of angular regions with intensities $\pm 3\sigma$ from the average in the same slant depth as reported in the Appendix. Applications of this cut reduced our data sample by 33%, giving 2.62×10^6 muons in the final sample.

We explored the effects of the main sources of systematics. The use of an average rock density (estimated using the results of the borehole surveys of the mountain) instead of a function depending on the zenithal and azimuthal angles, contributes $\sim \pm 1.5\%$ to the rock thickness, corresponding to $\sim \pm 5\%$ on the muon intensity at 3200 hg cm^{-2}. A further $\sim$ 5% contribution to the absolute scale of the muon intensity comes from the assumption of a homogeneous mountain instead of a layered structure as modelled in Reference [10] and described in [8]. The total systematic uncertainty is thus estimated at $\pm$ 8%.

In the range 3200 - 7000 hg cm^{-2} the data are well fitted by the three parameter empirical formula

$$I(h) = A \left(\frac{h_0}{h}\right)^{\alpha} e^{-\frac{h}{h_0}} \tag{2}$$

where A = $(1.96 \pm 0.03) \times 10^{-6}$ cm^{-2}s^{-1}sr^{-1}, $\alpha = 1.10 \pm 0.01$ and $h_0 = (972 \pm 3)$ hg cm^{-2} with a χ^2/DoF = 65/51. Using the Frejus [9] function

$$I(h) = B \left(\frac{h_1}{h}\right)^{2} e^{-\frac{h}{h_1}} \tag{3}$$

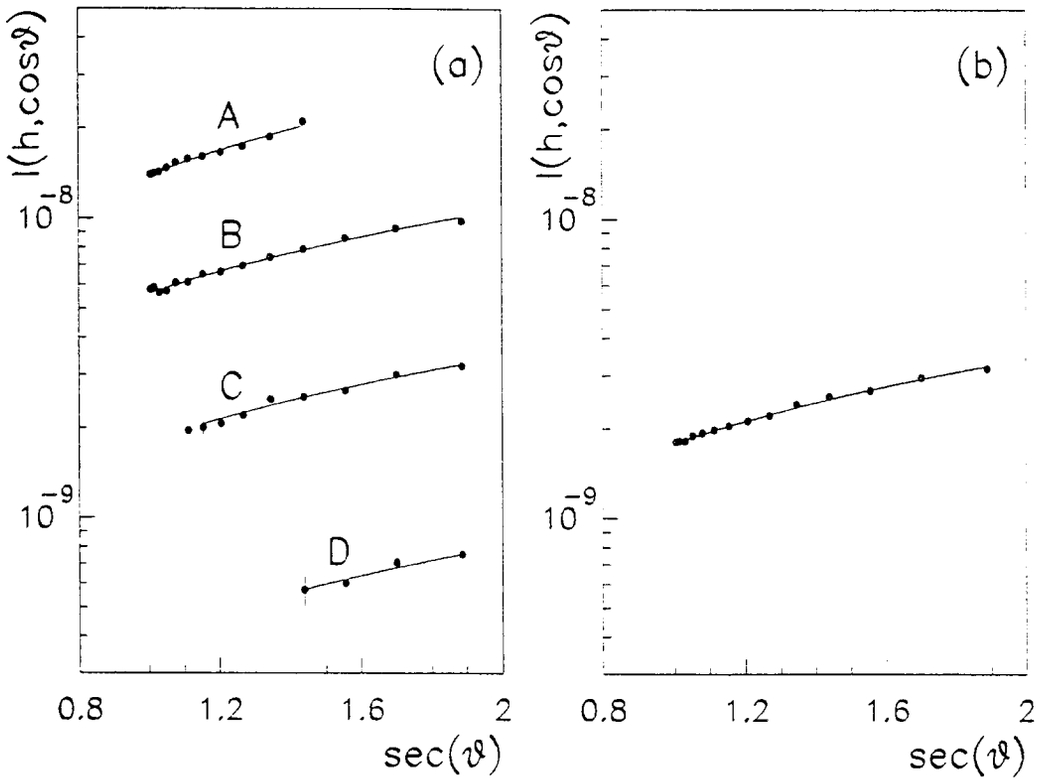

Figure 2: (a) The vertical muon intensity versus $1/\cos(\theta)$ is presented for 4 ranges of rock depth: A) 3150 - 3750; B) 3850 - 4550; C) 4650 - 5550; D) 5650 - 6950 hg cm^{-2}. (b) The data shown in part (a) are scaled to h = 5400 hg cm^{-2}. Data are plotted in logarithmic scale.

in the same range, we obtain B = $(1.81 \pm 0.06)\times10^{-6}$ cm^{-2}s^{-1}sr^{-1} and h_1 = (1231 $\pm$1) hg cm^{-2} with a $\chi^2/DoF = 76/52$, and a correlation coefficient between h_1 and B of -0.909. The errors quoted for the fitted parameters account for the statistical uncertainties and the Gran Sasso map resolution of $\sim$ 10 m. Figure 2 shows the behaviour of the intensity as a function of sec(θ) at fixed depth. In Figure 2a the data were binned in four depth regions of rock and in Figure 2b the experimental points are scaled to the central slant depth value h = 5400 hg cm^{-2} from the empirical relation (2). The errors are due to statistics and to the resolution of the topographical map; the systematic contributions related to the mountain knowledge are not included. The linear behaviour of the data is an *a posteriori* confirmation of the angular dependence of the underground muon intensity assumed in (1).

In Figure 3a our data are compared to a summary of world data in the range 1000 - 17000 hg cm^{-2}; Figure 3b is a blow up of the slant depth region relevant to our present results. Our data agree within the combined statistical and systematic uncertainties with the data of other experiments. In Figure 3b our fit is compared to data fits of other experiments and to the Crouch compilation presented at the Moscow 87 ICRC [11]. A difference of about 40% is found between MACRO and NUSEX fits where our data overlap [16]. The Frejus fit [9] differs from ours by $\sim$ 10 - 15%; which is within one standard deviation of their fitted parameters. The comparison of our data with the

Crouch compilation shows differences of less than 6% over this range. The observed discrepancies with NUSEX might be connected to unknown systematic uncertainties in their rock overburden.

3. Primary Spectrum

In the context of the superposition model, the muon flux at the surface contains information on the "all-nucleon" primary spectrum $N(E_p)$, and this information is mediated through the details of the hadronic interactions and meson lifetimes. In the energy range relevant for the present measurement (10 – 200 TeV/nucleon), the relation between the uncorrelated muon flux and the "all-nucleon" spectrum is approximated as reported in Reference [1] by the following:

$$\frac{dN_\mu}{dE\ d\Omega} \simeq N(E)\frac{Z_{N\pi}}{1-Z_{NN}}\frac{\left[1-(r_\pi)^{\gamma+1}\right](1-r_\pi)^{-1}(\gamma+1)^{-1}}{1+\frac{B_\pi cos\theta E}{\epsilon_\pi}} \tag{4}$$

where:

$$B_\pi = \frac{(\gamma+2)}{(\gamma+1)}\frac{1-(r_\pi)^{\gamma+1}}{1-(r_\pi)^{\gamma+2}}\frac{\Lambda_\pi-\Lambda_N}{\Lambda_\pi ln\,(\Lambda_\pi/\Lambda_N)}$$

$$r_\pi = \left(\frac{m_\mu}{m_\pi}\right)^2.$$

Equation (4) is summed over kaon decay channels as well, where we define B_K and r_K in a similar fashion. The constant $\epsilon_{\pi,K}$ contains the meson lifetimes and depends on the structure of the atmosphere; Z_{ij} are the spectrum averaged moments , which in principle may depend on the energy; they contain information on the inclusive distribution as well as the primary spectrum; Λ_i are the atmospheric attenuation lengths.

Assuming for the "all-nucleon" spectrum a simple power dependence

$$N(E) = N_0 E^{-\gamma_p}$$

(which is well established in the energy range pertaining to this measurement) both the spectral index, γ_p, and normalization, N_0, can be derived from the vertical intensity, after the spectrum averaged moments and interaction lengths (as well as details of the atmosphere) are deduced from a Monte Carlo code. In the approximation of exact Feynman scaling and a single power spectrum, the spectrum averaged moments and interaction lengths are constant.

We estimated the "all-nucleon" spectrum by the least square method to unfold $N(E)$ from the measured underground intensity defined by:

$$I(h) = \int d\Omega \int_0^\infty \frac{dN_\mu}{dE\ d\Omega} P(E,h)dE \tag{5}$$

with h the rock depth, $\frac{dN_\mu}{dE\ d\Omega}$ the muon intensity at the surface, $P(E,h)$ the survival probability, and the angular integration is performed at constant slant depth. The survival probabilities were calculated for surface muons with energies in the 1 – 100 TeV energy range, using a GEANT code especially tuned for the Gran Sasso rock. The

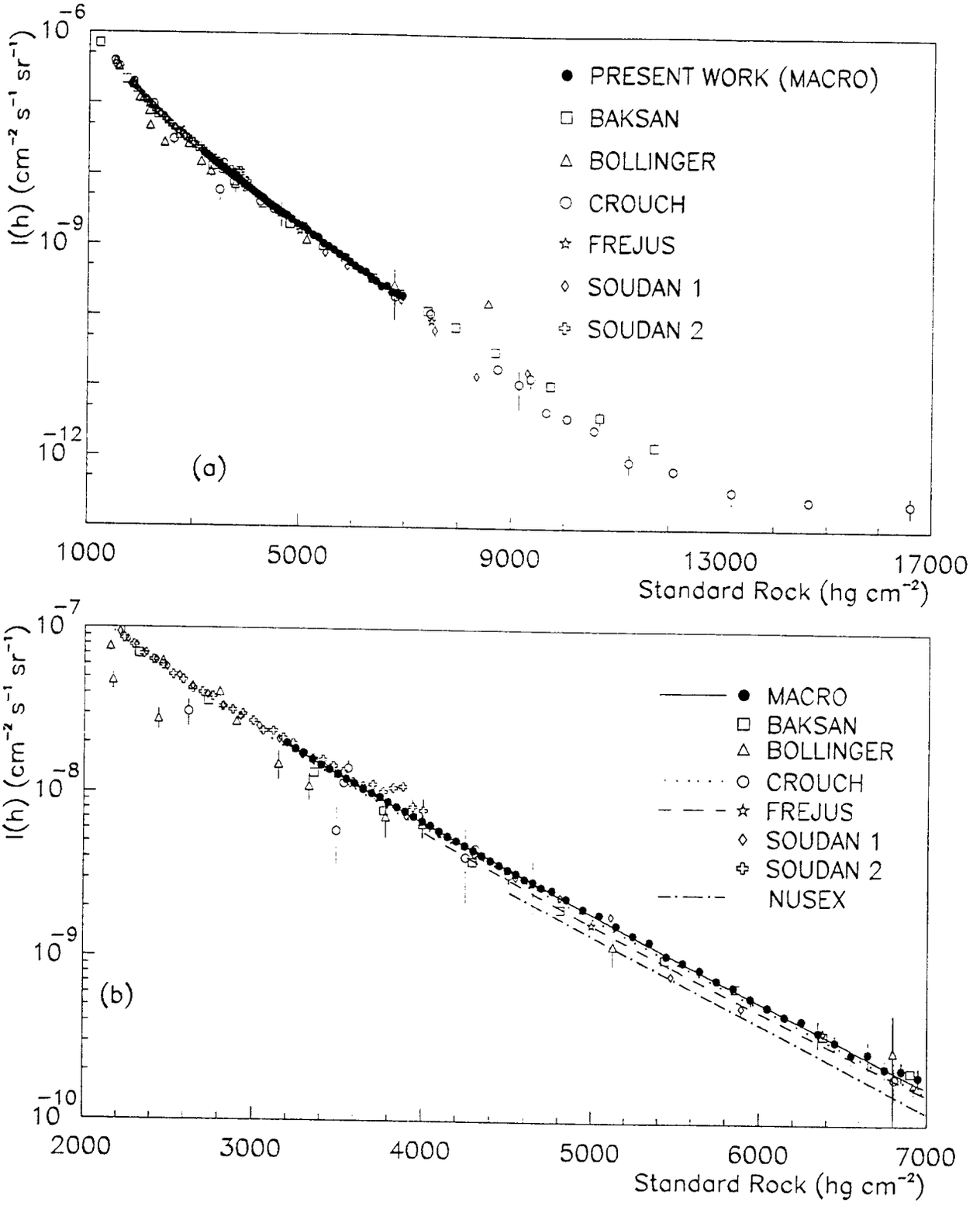

Figure 3: Vertical muon intensity versus standard rock. (a) The present MACRO results are superimposed on the data compiled by Crouch [11] and those collected by other experiments : Baksan [12], Bollinger [13], Frejus [9], Soudan 1 [14], Soudan 2 [15]. (b) The region covered by our data is shown in more detail. The solid line is the fit of our data according to Equation (2); the dotted line is the Crouch fit [11]; the dashed line is the Frejus fit and the dash-dotted line the NUSEX fit.

	INPUT			OUTPUT	
Model	Z_{NN}	$Z_{N\pi}$	Z_{NK}	N_0 $(cm^{-2}s^{-1}sr^{-1}GeV^{\gamma_p-1}A)$	γ_p
Gaisser	0.298	0.079	0.0118	3.4 ± 0.1	2.78 ± 0.04
Hemas	0.26	0.057	0.0113	5.0 ± 0.1	2.79 ± 0.04
Sibyll	0.28	0.068	0.0071	4.1 ± 0.1	2.77 ± 0.05
	Λ_N	Λ_π	Λ_K		
All models	120	160	180		

Table 2: Spectrum weighted moments (Z_{ij}) and atmospheric attenuation lengths (Λ_i in g cm^{-2}) for hadrons, and all nucleon spectrum results fitted for the three adopted models.

code includes a detailed description of muon propagation underground, and accounts for fluctuations in muon energy losses [8].

We used different sets of Z_{ij} functions derived from three interaction models: a) one from Reference [1], which are constant as a function of energy since Feynman scaling is assumed to be exact, b) the HEMAS interaction model [26] and c) the SIBYLL interaction model [27]. In the latter two cases the Z functions exhibit a smooth dependence on primary energy, since scaling violations are included in the quoted models. We have chosen the values at 10 TeV/nucleon, since this is roughly the most probable energy of primaries that produce the inclusive muon flux at MACRO depth. The numerical values of these parameters are listed in Table 2.

The fit of our data using the three models gives the spectral index γ_p and the primary normalization factor for the values listed in Table 2. The correlation coefficient between γ_p and N_0 is 0.975. The errors include both the statistical and the map resolution uncertainties. Further uncertainties of the order 5% in N_0 and 3% in γ_p must be considered as discussed in the next section. The spread of the three values gives an estimate of the uncertainties of the magnitude of the primary flux due to the interaction model. Our evaluations are in good agreement with the estimation reported in [28]. The results in Table 2 should be considered in light of the following comments. We notice that the Z functions from HEMAS and SIBYLL, used to reproduce the observed underground muon intensity, produce a reconstructed all-nucleon spectrum higher than what can be obtained from the average of the existing direct measurements in the range 1 – 100 TeV[29]. This is consistent with the analysis of the muon multiplicity distributions by MACRO[30], where a full simulation using the HEMAS code gave an absolute rate of events which is lower by a factor of 25% with respect to the experimental data.

4. Muon flux at the surface

In order to evaluate the surface muon flux, we have chosen the parameters of the model described in Reference [1], which yields the following formula:

$$\frac{dN_\mu}{dE\ d\Omega} = A \times E^{-\gamma} \times \left(\frac{1}{1 + \frac{1.1E\ cos\theta}{115\ GeV}} + \frac{0.054}{1 + \frac{1.1E\ cos\theta}{850\ GeV}} \right). \quad (6)$$

We have used the same method described in Section 3 to solve for A and γ. The result of this procedure gives the following values: $A = (0.26 \pm 0.01)$ cm^{-2} s^{-1}sr^{-1} GeV$^{\gamma-1}$; $\gamma = 2.78 \pm 0.01$ with a $\chi^2/\mathrm{DoF} = 41/52$ (Φ is in cm^{-2} s^{-1} sr^{-1} GeV^{-1}, and E is in GeV). The errors are due to statistics and the map resolution. The fitted parameters are also affected by uncertainties of the rock density and the hard energy loss cross sections used to estimate the survival probabilities. The effect of the uncertainty in the rock density produces a variation of 3.5% in A and less than 1% in γ. Because there are uncertainties in the bremsstrahlung and photonuclear cross sections, as pointed out in [17], the results obtained here also depend upon the cross sections of the stochastic radiative processes used in GEANT. We used different sets of survival probabilities to test the sensitivity of the fitted parameters to these uncertainties. Using the energy losses described in [18], where a different photoproduction cross section is employed [19] we obtain a variation of $\simeq 2\%$ in both A and γ but with a $\chi^2/\mathrm{DoF} = 2.9$. We estimate the overall systematic errors resulting from rock density and hard energy loss cross sections to be $\sim 5\%$ in A and $\sim 3\%$ in γ.

As pointed out in Reference [20], the vertical sea level muon spectrum is not well known at energies greater than a few hundred GeV and even for energies below this range, the statistical and systematic errors of existing experiments are quite large ($\pm$10 – 15 % range). Hence our high statistics measurements of the surface muon flux in the energy range from 1 – 20 TeV provide much needed new information on the high energy dependence of the sea level muon spectrum. In Figure 4a we present a collection of world data on the surface muon differential flux versus energy. The fit through our data points is represented by the continuous line. In Figure 4b the same data are presented multiplied by E_μ^3 in order to eliminate the energy dependence on the flux behaviour. Our fit agrees well with the high energy measurements at sea level. The same figure also shows the differential flux calculation of Reference [1]. A maximum difference of 10 % from our result is observed at 1 TeV. Our data provide new information on the flux of muons above 1 TeV and agree well with the predictions of Reference [1].

5. Conclusions

We measured the underground muon intensity as a function of the slant depth, in the range 3000 – 7000 hg cm^{-2}, with the MACRO detector. The average parameters of the rock were estimated using the material extracted during the tunnel excavation and the mountain surveys as described in the Appendix. The high statistics of this data sample allowed identification of regions where the mountain map is not well known. Our vertical muon intensities agree well with the SOUDAN and BAKSAN data and the world compilation of Reference [11], while the Frejus [9] and the NUSEX [16] data are lower. The differences here are likely due to different methods of measurements in each of the experiments and uncertainties in the knowledge of overburden composition in the three experiments.

Using three different nuclear interaction models the primary "all-nucleon" spectrum has been evaluated in the energy range 10 – 200 TeV/nucleon. The spectral index is almost model independent while the spread in the absolute normalization is of the order of 25%, larger than the statistical uncertainty. Also, from our data we determined the

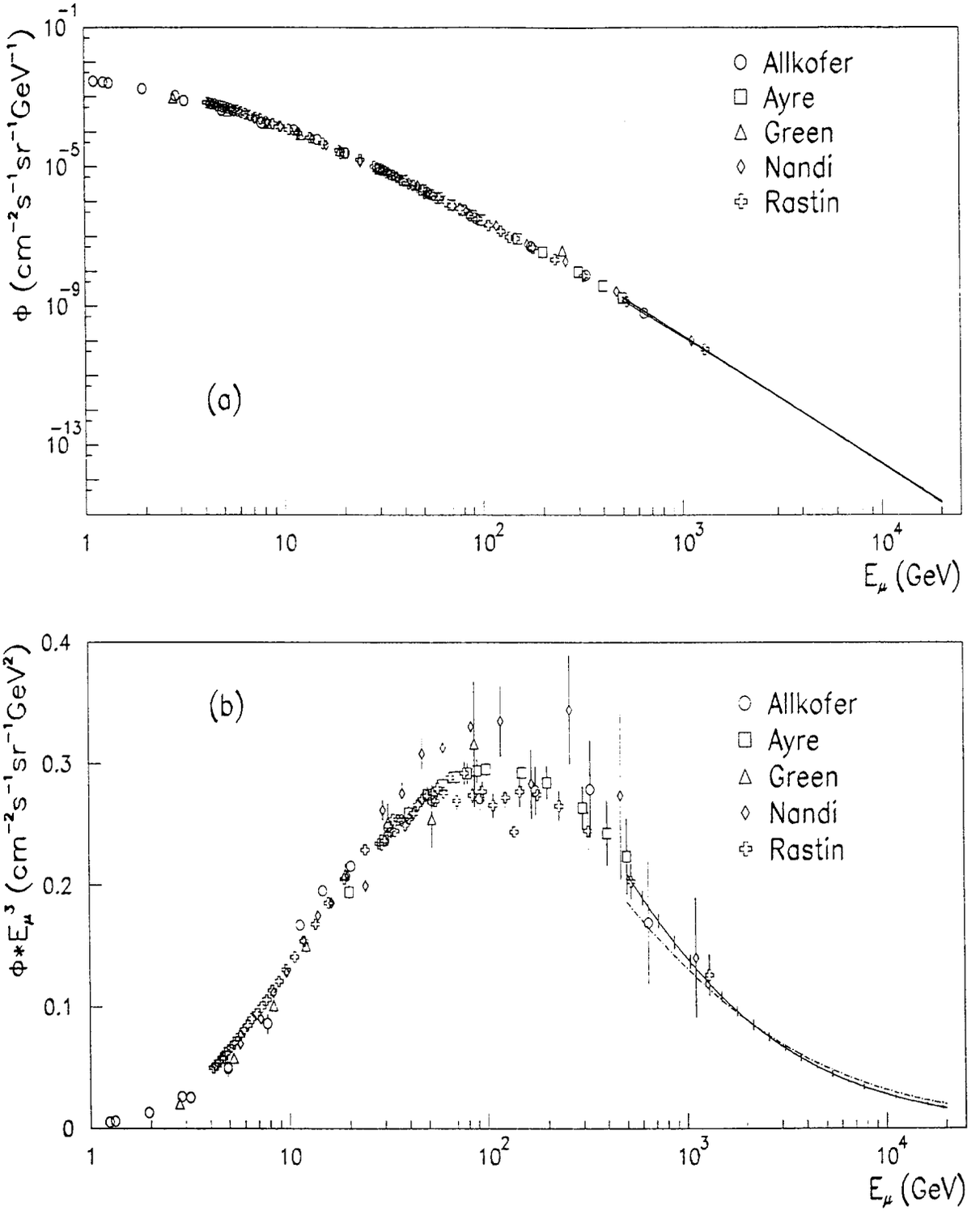

Figure 4: (a) Differential muon energy flux at the surface. The MACRO fit reported in the text (solid line) is superimposed to the available experimental measurements : Allkofer [21], Ayre [22], Green [23], Nandi [24], Rastin [25]. (b) $E_\mu^3 \Phi(E_\mu)$ is shown as a function of E_μ. The solid line shows the fit of formula 6; the dash-dotted line the calculated formula pg. 71 of [1]. The vertical bars represent one standard deviation on the parameters of the fitted intensity.

surface muon flux. For muon energies larger than $\sim$ 1 TeV, our data agree well with the analytical estimate reported in [1].

The use of the MACRO detector with full acceptance will allow a considerable statistical improvement for angular regions larger than 60°, extending the statistics for depths greater than 7000 hg cm^{-2}, then to primary cosmic ray energies up to the knee region.

6. Acknowledgements

We gratefully acknowledge the support of the director and of the staff of the Laboratori Nazionali del Gran Sasso and the invaluable assistance of the technical staff of the Institutions participating in the experiment. We thank the Istituto Nazionale di Fisica Nucleare (INFN), the U.S. Department of Energy, and the U.S. National Science Foundation for their generous support of the MACRO experiment. We thank INFN for providing fellowships and grants (FAI) for non italian citizens.

Appendix: Characteristics of the Gran Sasso rock

The rock surrounding the Gran Sasso underground laboratory has a quite irregular structure; its composition is essentially calcareous, mixed with other materials, such as aluminum, silicon, magnesium compounds and organic remains. We made detailed analyses of the material found during the tunnel excavation to study the rock structure, and to make a composition and density model of the Gran Sasso rock [10]. The chemical composition results are shown in Table 3.

The average values of the elemental composition parameters were calculated in the angular range 0° – 60°; they are very close to the standard rock values (see Table 4). The Gran Sasso rock thicknesses as obtained from the digitization of the mountain topographic map supplied by the Italian Military Geographical Institute (IGM), as a function of the zenith and the azimuth angles, are given in Tables 5 and 6. The azimuth is measured relative to geographic North. The topographic map is not completely reliable everywhere and the empty bins represent regions where the rock is poorly known. In order to identify those regions, we employed both underground muon intensity measured with the MACRO detector using (1) and the topographic survey.

rock type	chemical composition	% Weight
dolomite	$CaCO_3(90\%), MgCO_3(10\%)$	50
dolomite limestone	$CaCO_3(50\%), MgCO_3(50\%)$	29
flint limestone	$CaCO_3(72\%), SiO_2(8\%),$	
	Si, Al, K compounds (20 %)	8
karst formation	$CaCO_3$	9
detritus	$CaCO_3(49\%), MgCO_3(1\%),$	
	Si, Al, K compounds (50 %)	3

Table 3: Gran Sasso rock chemical composition (Reference [10]).

A = 22.87	Z = 11.41	density = (2.71 ± 0.05) g cm^{-3}	
Chemical element	Atomic Number	Atomic Weight	Relative Weight
Hydrogen	1	1.008	0.03
Carbon	6	12.011	12.17
Oxygen	8	15.99	50.77
Magnesium	12	24.305	8.32
Aluminium	13	26.981	0.63
Silicon	14	28.085	1.05
Potassium	19	39.098	0.10
Calcium	20	40.078	26.89

Table 4: Gran Sasso rock average parameters. They are very similar to the so called Standard Rock for which A = 22; Z = 11 and $\rho = 2.65$ g cm^{-3} .

Azimuth	Zenith angle (degrees)											
(deg.)	5	10	15	20	25	30	35	40	45	50	55	60
0	1338	1302	1326	1292	1268	1292	1316	1324				
5	1339	1303	1302	1272	1244	1267	1303	1304				
10	1341	1305	1287	1254	1224	1246	1276	1295				
15	1343	1305	1278	1239	1216	1221	1238	1267				
20	1346	1307	1279	1237	1222	1240	1239	1234				
25	1349	1310	1280	1247	1248	1272	1263	1246				
30	1349	1313	1285	1271	1279	1309	1270	1277				
35	1350	1317	1291	1296	1301	1298	1303	1310				
40	1354	1323	1312	1320	1311	1311	1335	1343				
45	1361	1336	1335	1341	1326	1344	1352	1377				
50	1370	1350	1362	1374	1350	1372	1371	1378				
55	1376	1359	1386	1406	1375	1364	1380	1378				
60				1414	1380	1352	1366	1370				
65				1401	1374	1337	1350	1377				
70				1390	1365	1347	1366	1383	1438	1487	1539	1597
75				1388	1371	1371	1384	1419	1471	1516	1562	1659
80				1398	1387	1388	1406	1465	1496	1533	1639	1774
85				1411	1405	1414	1448	1480	1501	1592	1726	1869
90				1420	1426	1446	1481	1495	1547	1674	1804	1908
95				1401	1400	1430	1472	1513	1585	1649	1754	1904
100	1381	1367	1353	1380	1372	1395	1435	1482	1545	1598	1668	1805
105	1377	1358	1328	1352	1361	1353	1401	1427	1486	1557	1615	1760
110	1371	1350	1311	1330	1335	1345	1355	1398	1440	1495		
115	1367	1341	1302	1308	1310	1317	1320	1351	1392	1455		
120	1362	1330	1291	1280	1283	1286	1299	1317	1362	1431		
125	1356	1314	1284	1244	1255	1255	1269	1291	1338	1410		
130	1354	1304	1277	1232	1233	1234	1251	1268	1318	1397		
135	1350	1287	1268	1229	1211	1214	1225	1255	1306	1380		
140	1348	1287	1260	1223	1204	1199	1216	1246	1302	1375		
145	1346	1284	1250	1220	1193	1190	1207	1244	1296	1370		
150	1348	1283	1238	1215	1186	1182	1200	1241	1295	1371		
155	1347	1280	1235	1205	1179	1173	1200	1237	1297	1371		
160	1345	1277	1230	1203	1176	1168	1197	1236	1299	1378	1536	1764
165	1346	1271	1229	1193	1172	1164	1196	1242	1297	1385	1562	1885
170	1348	1269	1228	1185	1167	1166	1196	1250	1306	1401	1577	1974
175	1349	1268	1227	1188	1166	1165	1196	1256	1320	1414	1599	2146
180	1350	1268	1224	1192	1169	1166	1203	1260	1333	1429	1634	2142
185	1348	1268	1222	1185	1173	1171	1208	1265	1347	1451	1670	2168
190	1347	1266	1220	1183	1170	1178	1216	1271	1347	1470	1704	2085
195	1342	1260	1220	1187	1172	1186	1222	1288	1363	1486	1716	2096
200	1339	1264	1218	1186	1180	1193	1232	1298	1376	1504	1727	2023

Table 5: Rock thickness (m) as a function of zenith and azimuth. The table indicates the regions in the mountain where the slant depth of the overburden is known with confidence.

Azimuth	Zenith angle (degrees)											
(deg.)	5	10	15	20	25	30	35	40	45	50	55	60
205	1345	1266	1216	1191	1188	1203	1241	1299	1384	1521	1738	2016
210	1349	1272	1227	1198	1194	1218	1254	1307	1398	1559	1781	2243
215	1352	1277	1239	1204	1207	1228	1262	1322	1406	1575	1866	2239
220	1354	1282	1246	1210	1218	1240	1274	1334	1422	1597	1951	2227
225	1356	1292	1254	1223	1230	1260	1301	1356	1456	1637	1989	2220
230	1359	1308	1264	1251	1244	1280	1331	1397	1484	1665	2008	2225
235	1363	1322	1278	1269	1263	1285	1340	1415	1497	1679	2051	2209
240	1371	1337	1296	1292	1283	1300	1348	1424	1537	1741	2105	2286
245	1379	1337	1317	1313	1300	1317	1360	1440	1583	1784	2195	2520
250	1385	1341	1346	1332	1318	1343	1382	1462	1638	1843	2353	2630
255	1392	1348	1366	1349	1342	1369	1422	1523	1766	2042	2454	2714
260	1396	1364	1388	1368	1368	1396	1454	1567	1921	2178	2324	2520
265				1388	1396	1426	1476	1581	1968	2056	2195	2369
270				1409	1433	1457	1505	1587	1889	2021	2120	2303
275				1439	1470	1499	1538	1616	1890	2012	2133	2346
280				1465	1499	1526	1560	1639	1897	1998	2177	2394
285				1499	1523	1560	1579	1656	1888	1996	2199	2426
290				1532	1560	1585	1611	1713	1895	2016	2195	2462
295	1360			1569	1591	1622	1656	1773	1916	2035	2218	2481
300	1354			1597	1636	1661	1711	1849	1957	2065	2254	2609
305	1348			1580	1661	1699	1767	1857	1958	2094	2282	2784
310	1345			1543	1642	1742	1797	1866	2002	2147	2293	2835
315	1341			1511	1599	1742	1808	1900	2046	2206	2452	2937
320	1337			1477	1549	1696	1773	1887	2115	2302	2773	2960
325	1334					1651	1700	1815	2213	2571	2833	2902
330	1333					1598	1643	1738	2217	2758	2840	2922
335	1334					1537	1587	1712	2386	2723	2892	3022
340	1334					1451	1519		2253	2692	2894	3038
345	1334					1385	1460		1970	2494	2823	2967
350	1335			1326	1322	1346	1408		1890	2486	2585	2881
355	1335			1313	1295	1320	1350		1685	2180	2417	2632

Table 6: Rock thickness (m) as a function of zenith and azimuth. The table indicates the regions in the mountain where the slant depth of the overburden is known with confidence.

References

[1] T. Gaisser, *Cosmic Rays and Particle Physics*, Cambridge University Press (1990).

[2] C Castagnoli *et al.*, Nuovo Cimento A, **82**, 78(1984); A. Castellina *et al.*, Nuovo Cimento C, **8**, 93(1985).

[3] L. Bergamasco *et al.*, Nuovo Cimento C, **6**, 596(1983).

[4] S.P. Ahlen *et al.*, Nucl. Instrum. Methods A, **234**, 337(1993).

[5] S.P. Ahlen *et al.*, Phys. Lett. B, **249**, 149(1990).

[6] R. Brun *et al.*, CERN GEANT 3 USER'S GUIDE DD/EE/84-1 (1987,1992).

[7] Yu. D. Kotov and V. M. Logunov, 11th ICRC, Budapest, MU-50 (1969).

[8] H. Bilokon *et al., Muons survival probabilities in the Gran Sasso Rock*, LNGS - 94/92, (1994).

[9] Ch. Berger *et al.*, Phys. Rev. D, **40**, 2163(1989).

[10] P.G. Catalano, *Caratteristiche geolitologiche e strutturali dell'ammasso roccioso sovrastante il laboratorio I.N.F.N.*, ANAS report (1986); P.G. Catalano et al., Mem. Soc. Geol. It., **35**, 647(1986).

[11] M. Crouch, 20th ICRC, Moscow, **HE 4.1-2** (1987).

[12] Y.M. Andreyev, V.I. Gurentsov and I.M. Kogai, 20th ICRC, Moscow, **HE 4.1-19**, (1987).

[13] P.H. Barrett *et al.*, Rev. Mod. Phys., **24**, 133(1952). L. M.Bollinger, Phys. Rev. A, **79**, 207(1950).

[14] K. Ruddick, private communication and Soudan collaboration Int. Report PDK-435, (1990), (unpublished).

[15] Susan M. Kasahara Ph. D. Thesis, University of Minnesota (unpublished).

[16] M. Aglietta *et al.*, Nucl. Phys. B (Proc. Suppl.), **14**, 193(1990).

[17] R.P. Kokoulin and A.A. Petrukin, 22nd ICRC, Dublin, **HE 4.1.3** (1991).

[18] P. Lipari and T. Stanev, Phys. Rev. D, **44**, 3543(1991).

[19] W. Lohmann, R. Kopp and R. Voss, *Energy loss of muons in the energy range 1–10000 GeV*, CERN 85-03 (1985).

[20] D.H. Perkins, Nucl. Phys. B, **399**, 3(1993).

[21] O.C. Allkofer, K. Carstensen and W.D. Dau, Phys. Lett. B, **36**, 425(1971).

[22] C.A. Ayre *et al.*, J. Phys. G, **1**, 584(1975).

[23] P.J. Green *et al.*, Phys. Rev. D, **20**, 1598(1979).

[24] B.C. Nandi and M.S. Sinha, J. Phys. A, **5**, 1384(1972).

[25] B.C. Rastin, J. Phys. G, **10**, 1609(1984).

[26] C. Forti *et al.*, Phys. Rev. D, **25**, 3668(1990).

[27] R.S. Fletcher, T.K. Gaisser, P. Lipari, T. Stanev, Bartol Research Institute BA-94-01, Jan 1994. Submitted to Phys. Rev. D.

[28] L. Bergamasco *et al.*, Nuovo Cimento C. **6**, 569(1983).

[29] S. Swordy, 23rd ICRC, Calgary, Invited, Rapporteur & Highlight papers, 243 (1993).

[30] M. Ambrosio *et al.*, (MACRO Collaboration), 23rd ICRC, Calgary, 2, 97 (1993).